Phys Chem Minerals (1983) 9:79–94

PHYSICS AND CHEMISTRY OF MINERALS

The Mechanisms of the Formation and Growth of Water Bubbles and Associated Dislocation Loops in Synthetic Quartz

A.C. McLaren, R.F. Cook, S.T. Hyde, and R.C. Tobin
Department of Physics, Monash University, Clayton, Victoria, Australia, 3168

Abstract. The development of water bubbles in synthetic quartz has been monitored by measurements of (i) the intensity of the light scattered and (ii) the increase in volume of the crystal, both as a function of temperature and time. These macroscopic measurements have been complemented by observations of the resulting microstructures, using *transmission electron microscopy* (TEM). A mechanism is proposed on the assumption that hydrogen is incorporated in the quartz structure by means of $(4\,H)_{Si}$ defects. On heating, these defects diffuse and clusters develop. A cluster of $n(4\,H)_{Si}$ produces a water bubble of $(n-1)H_2O$, without any change of volume of the crystal. At any temperature T there is a critical bubble diameter above which the "steam" pressure P exceeds the pressure p for a spherical bubble in mechanical equilibrium. If P becomes greater than p, then the bubble increases in volume until $P=p$, the increase in volume being achieved by the pipe diffusion of Si and O away from the bubble site into a linked edge dislocation loop. This process produces the observed increase in volume of the crystal. The two diffusion processes take place virtually simultaneously and continue until all the $(4\,H)_{Si}$ defects have been trapped in the bubbles. Values of the diffusion constant and the activation energy for the diffusion of the $(4\,H)_{Si}$ defects are deduced. The relevance of these observations to the hydrolytic weakening of quartz is briefly discussed.

Introduction

Since the discovery of hydrolytic weakening of quartz by Griggs and Blacic (1965), many experimental studies have been made of the plastic deformation of H-rich synthetic quartz, and these have recently been reviewed by Paterson and Kekulawala (1979). Hobbs et al. (1972) showed that in general hydrogen affects the mechanical behaviour and strength of quartz by its influence (a) on the Peierls stress and hence the glide of dislocations, and (b) on the various factors that affect strain-hardening, in particular, recovery due to dislocation climb which is controlled by the diffusion of Si and O. Thus, in order to understand the role of hydrogen in these processes, it is necessary to know how hydrogen is incorporated into the quartz structure.

The infrared absorption spectra of clear, colourless, natural quartz crystals often exhibit sharp, dichroic absorption peaks in the 3 μm region some of which appear to be associated with H^+ acting as a charge compensator in the substitution of Al^{3+} for Si^{4+} (see, for example, Brunner et al. 1961; Kats 1962; Bambauer et al. 1963). These absorption peaks have also been observed in synthetic quartz, but they are often superimposed on a broad, isotropic absorption band extending from about 3,700 cm^{-1} to 2,600 cm^{-1} (see Wood 1960; Kats 1962; Dodd and Fraser 1965). Paterson and Kekulawala (1979) found that a similar broad band is commonly observed in Brazilian amethyst quartz.

In a survey of a wide range of quartz crystals, Kekulawala et al. (1981) observed hydrolytic weakening only in those crystals which exhibited the broad isotropic absorption band. From this they concluded that the hydroxyl species responsible for hydrolytic weakening absorb in this band, although they did not suggest a model for the incorporation of hydrogen in the quartz structure.

Another characteristic of quartz crystals which exhibit this broad isotropic absorption band is that on heating at atmospheric pressure at temperatures from about 500° C, they become milky due to light scattering by submicroscopic bubbles (Dodd and Fraser 1966). Paterson and Kekulawala (1979) and Kekulawala et al. (1981) found that at liquid N_2 temperatures such crystals exhibited a complex absorption band of intermediate width, peaking at 3,200 cm^{-1}, corresponding to the absorption of ice, presumably formed by the freezing of water in the bubbles. Transmission electron microscope observations by McLaren and Phakey (1966a) showed that the bubbles in amethyst quartz were about 200 to 1,000 Å in diameter and formed preferentially along the ubiquitous Brazil twin boundaries. However, bubbles linked by dislocations also developed between the boundaries. Since dislocations were never observed in the unheated crystals, it appeared that the bubbles and dislocations were introduced simultaneously. Subsequently, bubbles linked by dislocations were observed in heated synthetic quartz. Kekulawala et al. (1981) found that, on heating, the development of water bubbles significantly increased the strength of the crystals, presumably because the hydroxyl species responsible for hydrolytic weakening had been removed from the structure and converted to water in the bubbles.

Order of magnitude calculations by Phakey (1967) indicate that the bubbles are probably less than 20 percent filled with water. Therefore, since Si and O must have diffused away from the bubble site, space must have been created in the crystal and hence the crystal must have increased in volume. It follows that the process of bubble

0342-1791/83/0009/0079/$03.20

formation involves the diffusion of some sort of hydrogen defect and of Si and O. Since the diffusion of these species appears to be fundamental to the mechanism of hydrolytic weakening, a study of the kinetics of bubble formation has been made in the expectation that it will provide information about the nature of the hydrogen defect and of the mechanism of hydrolytic weakening.

The development of the bubbles has been monitored by measurements of the intensity of the light scattered and of the increase in volume of the crystals as a function of temperature and time. Since the diameter of the bubbles is significantly smaller than the wavelength λ of the light, the scattering is within the Rayleigh limit and the scattered intensity I_S is given by

$$I_S/I_0 = k\sum_i N_i^2 V_i/\lambda^4 \quad (1)$$

where I_0 is the intensity of the incident beam, N_i is the concentration of bubbles each of volume V_i and k is a constant (Kerker 1969). Although I_S is a function of both N_i and V_i (and the two cannot be separated), this technique does allow the development of bubbles to be monitored *continuously* as a function of temperature and time, so that an activation energy can be determined. On the other hand, the volume expansion was measured by multiple beam interferometry at room temperature *after* the crystal had been heated to a fixed temperature for a known time. However, such measurements are directly related to the integrated volume of the bubbles.

Whereas these measurements are concerned with the bulk effects and rates of bubble formation, *transmission electron microscopy* (TEM) has been used for the direct observation of the bubbles and associated dislocations. These TEM observations provide most of the essential evidence for a mechanism of bubble formation which is proposed on the basis that hydrogen is incorporated in the structure by point defects, each of which consists of a Si vacancy occupied by four H, written $(4\,H)_{Si}$. The proposed mechanism is in good qualitative and quantitative agreement with the bulk measurements and it implies that the rate-determining step in the process of bubble formation is the diffusion of the $(4\,H)_{Si}$ defects. The observations also provide an estimate of the value of the diffusion constant D.

A further significant aspect of the present study is that it appears to establish the $(4\,H)_{Si}$ defect as the "hydroxyl species" responsible for the hydrolytic weakening of quartz.

Experimental

Specimens

The observations described in this paper were made on specimens cut from the Z-growth sector of four Y-bar single crystals of synthetic quartz (designated *W*1, *W*2, *W*4 and *E*-1-1) and on specimens from three batches (designated 253, 256 and 270) of gem-quality crystals of amethyst quartz.

Specimens from the synthetic quartz crystals have been used in previous studies of the role of hydrogen in the deformation of quartz. Hobbs et al. (1972) used specimens from *W*1, *W*2 and *W*4, while Morrison-Smith et al. (1976) used crystal *W*2 only. More recently, Paterson and Kekulawala (1979) and Kekulawala et al. (1981) used specimens cut from *W*1, and *E*-1-1, as well as from crystals of amethyst quartz similar to those used here.

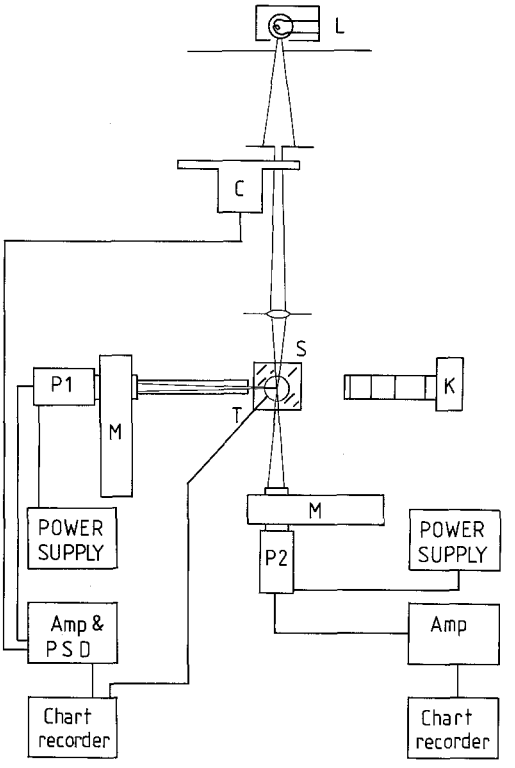

Fig. 1. Schematic diagram of the light-scattering apparatus

Light Scattering

The essential features of the light scattering apparatus are shown in Fig. 1. Light from an air-cooled, 150 W, quartz halogen lamp L was apertured twice before passing through a rotating-blade chopper C. The chopped beam was focussed by a 10 cm focal length lens onto the quartz specimen in the chamber of a hotstage S. The light scattered by the specimen at 90° to the incident beam passed through a collimating tube and a monochromator M to the photomultiplier $P1$. The output signal from $P1$ was processed by a phase sensitive detection system which ensured that only the component of the signal which was in phase with a reference signal from the chopper was averaged and amplified. In this way, a DC voltage was created which was proportional only to the intensity of the light scattered by the crystal. With this system, signals arising from room lighting and the glow of the hotstage at elevated temperatures were removed, as well as photomultiplier noise from all but a narrow bandwidth around the chopping frequency $f = 530$ Hz. By using this relatively high frequency, the flicker noise (which is proportional to $1/f$) due to semiconductor devices, was also reduced.

The transmitted beam was passed through a monochromator M to the photomultiplier $P2$. Since the intensity of the transmitted light was much greater than that of the scattered light, only a simple amplifier was used to process the output from $P2$.

The voltage associated with the scattered light, together with the voltage from a chromel-alumel thermocouple T

used to measure the temperature of the hotstage at a point immediately below the specimen chamber, were measured as a function of time on a two-channel chart recorder. A second recorder was used to measure the transmitted light intensity as a function of time.

The hotstage consisted of a vertically mounted cylindrical nickel rod 6 cm long and 2 cm in diameter. Nichrome heating coils (insulated with mica sheets) were wound on the rod both below and above the specimen chamber and alumina paste was baked over them. The specimen chamber was located about 2 cm from the top of the rod and was large enough to accommodate a rectangular block of specimen 10 mm long × 5 mm high × 4 mm wide which was oriented with its long dimension parallel to the incident beam. The entrance aperture and the diametrically opposite exit aperture were 3 mm in diameter and centred so that the straight-through beam passed through the centre of the specimen. This diameter was large enough not to aperture the beam, so clearly the beam diameter was significantly smaller than the width of the crystal. The specimen was inserted into the chamber from the exit side which was then blocked by a nickel plug containing the exit aperture. The exit aperture for the scattered light was 10 mm long and 2 mm high cut into the rod at the height of the straight-through beam. An aperture of this shape made it possible to measure the scattered intensity at various positions along the crystal. A similar exit aperture was cut on the other side of the hotstage so that the spatial distribution of the scattered intensity could be viewed directly or photographed with the camera K. The hotstage was supported in a firebrick thermal insulator by three horizontal pins fixed to the rod at the height of the centres of the apertures. By this means, any vertical movement of the apertures and specimen relative to the incident light beam, due to thermal expansion of the nickel rod, was reduced to a minimum. The end (5 mm × 4 mm) faces and the side (10 mm × 5 mm) faces of the crystals were polished to a good optical finish.

In the experiments where the intensities of the scattered and transmitted light were measured as a function of temperature and time, the monochromator for the scattered light was set at 5,000 Å with the slit at maximum width so that the scattered light measured was essentially not monochromated. The monochromator for the transmitted light was set at 5,000 Å with a relatively narrow slit width.

In the initial heating experiments it was observed that as the intensity I_S of the scattered light increased, the light transmitted by the crystal became noticeably red (as expected from the Rayleigh theory) and its intensity I_T decreased markedly.

If it is assumed that the observed decrease in I_T is due to scattering then we may write

$$I_T = I_0 e^{-\mu l} \qquad (2)$$

where

I_0 = intensity of the incident beam,

l = length of the crystal, and

$\mu = kNV^2/\lambda^4$, assuming ideal Rayleigh scattering.

Thus, assuming a homogeneous specimen, the transmitted intensity at the centre is given by

$$\begin{aligned} I_{TM} &= I_0 e^{-\mu l/2} \\ &= I_0 (I_T/I_0)^{1/2} \quad \text{from (2)} \\ &= I_0 T^{1/2}. \end{aligned} \qquad (3)$$

Hence, the intensity scattered at the centre of the crystal is given by

$$I_{SM} = I_{TM} \mu k' \qquad (4)$$

where k' is a constant.

It follows that the scattered intensity observed at the detector is given by

$$I_S = I_{SM} e^{-\mu w/2} \qquad (5)$$

where w is the width of the crystal, and hence

$$\begin{aligned} I_S &= I_{TM} e^{-\mu w/2} \mu k' \\ &= I_0 T^{1/2} \; e^{-\mu w/2} \mu k' \\ &= I_0 T^{1/2} \; T^{w/2l} \mu k'. \end{aligned} \qquad (6)$$

Now the true scattered intensity is $I_{SC} = I_0 \mu k'$, hence from (6)

$$I_{SC} = I_S T^{1/2} \; T^{-w/2l} \qquad (7)$$

For example, with $l = 10$ mm, $w = 4$ mm and $T = 0.1$, this correction gives

$$I_{SC} = 5 I_S.$$

All the observed scattering intensities I_S were corrected to I_{SC} by using Eq. (7).

Multiple Beam Interferometry (MBI)

The experimental arrangement for transmission MBI fringes was similar to that described by Tolansky (1960, 1968). Light of wavelength $\lambda = 5{,}460$ Å, obtained from a mercury lamp with the appropriate filter, was focussed by a condenser lens onto an iris diaphram (diameter ca. 1.5 mm) placed at the focus of a second lens which projected a parallel beam of light at normal incidence onto the interferometer plates. The resulting fringes were viewed or photographed through another lens. The interferometer consisted of a reference optical flat F and the quartz specimen Q which was initially polished optically flat. Both F and Q were coated on one side with a 400–450 Å thick layer of aluminium and clamped together in a simple *jig*. The optical flat F (with the aluminium coating upwards) was positioned centrally on a glass base with the quartz specimen Q (coating downwards) immediately above. A suitably sized rubber O-ring was placed between the quartz and an upper cover glass. By means of three independently-adjustable clamping screws, pressure was applied to the cover glass at three points symmetrically placed around the O-ring, but as far as possible away from the quartz plate to minimize warping. Thus, the position of the apex of the wedge between F and Q could be adjusted to give a suitable orientation and spacing of the fringes.

The quartz specimens were heated at various temperatures for various times either in the hotstage of the light scattering apparatus or in a large muffle furnace. Clearly, it was necessary to remove the aluminum coating before each heat-treatment; this was done by immersing the crystal in dilute nitric acid for no longer than 15 min.

Light Scattering Observations

Figure 2 shows the (uncorrected) scattered intensity I_S observed at the detector ($P1$ of Fig. 1) as a function of time and at various temperatures for a specimen $W2/1$. The temperature (as measured by the thermocouple reading) as a

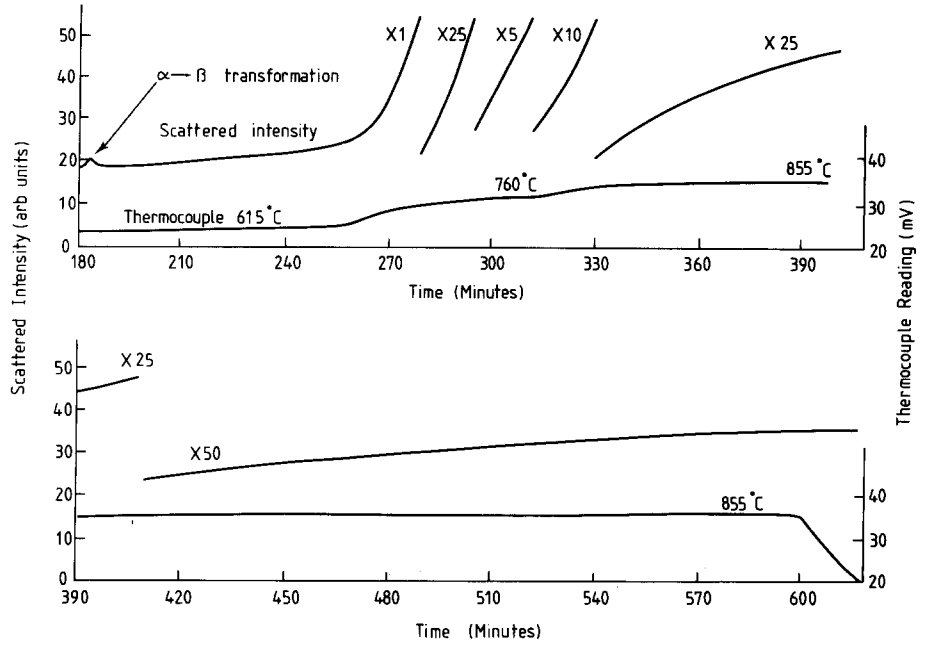

Fig. 2. Curve showing the uncorrected intensity I_s of the scattered light (as actually detected by the photomultiplier $P1$) as a function of time for the specimen $W2/1$, together with the corresponding thermocouple reading

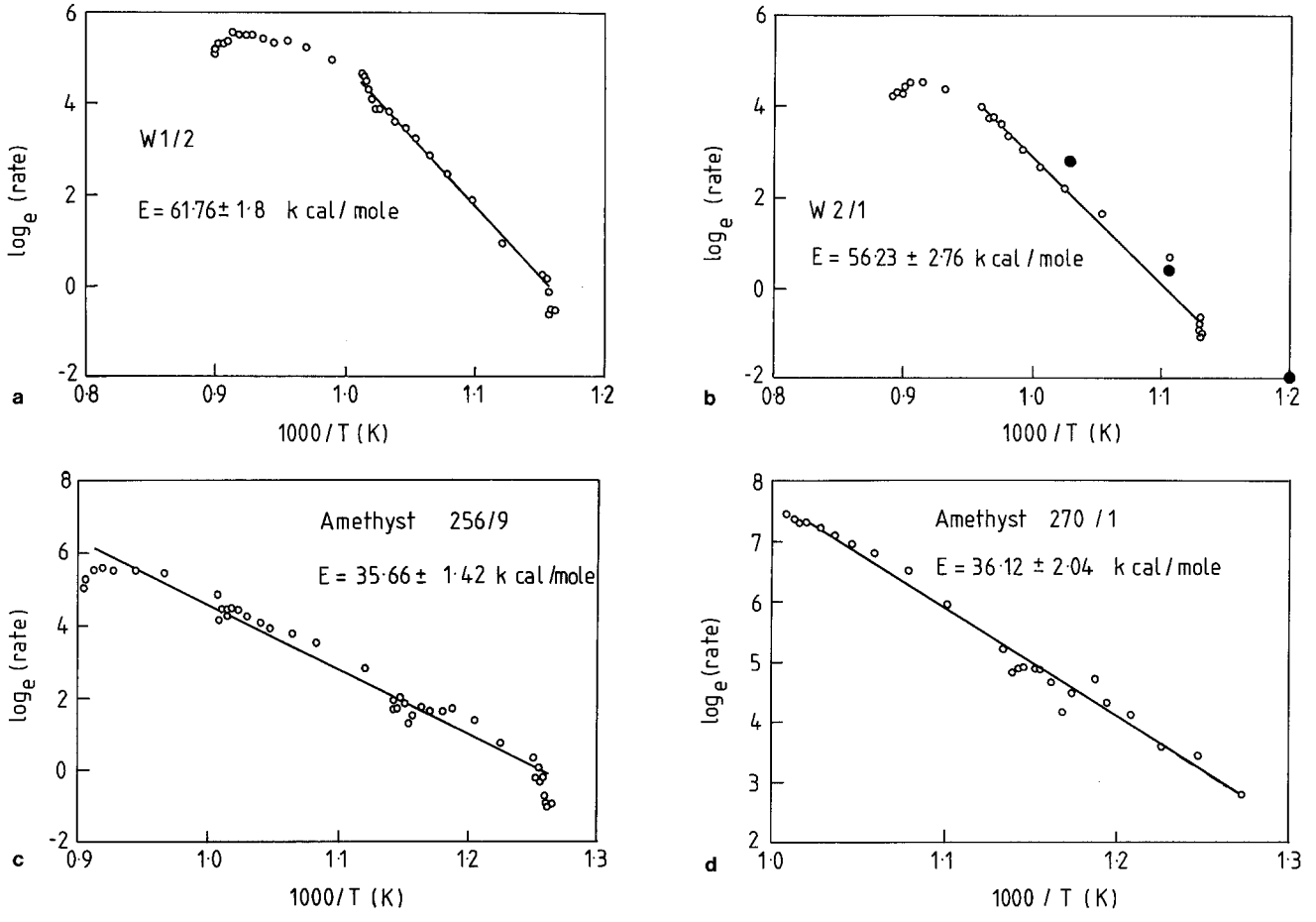

Fig. 3a–d. Arrhenius plots of $\log_e(\mathrm{d}I_{sc}/\mathrm{d}t)$ as a function of $1{,}000/T(\mathrm{K})$ determined from the light scattering measurements for two synthetic quartz specimens ($W1/2$ and $W2/1$) and two amethyst quartz specimens (256/9 and 270/1). The activation energy E determined from the straight line of best fit is shown for each specimen. The values of $\log_e(d\alpha/\mathrm{d}t)$, determined from the slopes of the lines of Fig. 6b, are also plotted as a function of $1{,}000/T(\mathrm{K})$ for specimen $W2/1$ (filled-in circles)

function of time is also shown. Note the small peak in the scattered intensity due to the $\alpha \rightarrow \beta$ transformation at 573° C after a heating time of about 183 min. It will be seen that I_S increases with time but eventually saturates at a constant value after about 600 min for this particular temperature program, and that this saturated value of I_S does not change when the crystal is cooled. Further, it will be seen that up to a temperature of about 800° C, the rate

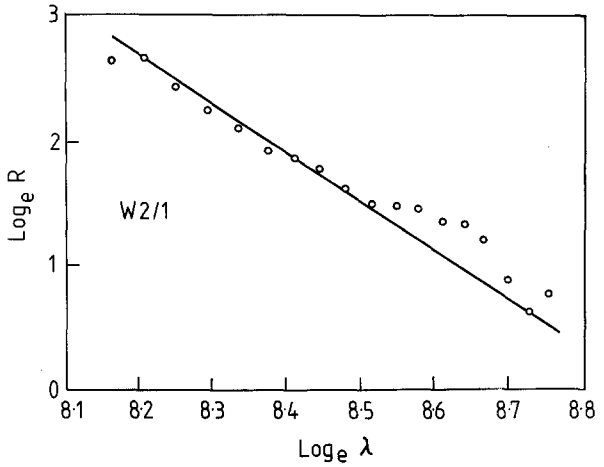

Fig. 4. The observed variation of the Rayleigh ratio $R = I_{sc}/I_0$ with wavelength λ for specimen $W2/1$ after heating to scattering saturation at 855° C. It will be seen that the points lie close to the straight line of slope −4.0, confirming that the conditions for Rayleigh scattering are reasonably well satisfied

of change of scattering dI_S/dt increases rapidly with increasing temperature.

From curves of the type shown in Fig. 2, graphs were plotted of $\log_e(dI_{SC}/dt)$ against the reciprocal of the absolute temperature T(K), where I_{SC} is the measured scattered intensity corrected for attenuation by Eq. (7). A four-point approximation was used to determine (dI_{SC}/dt) at each temperature point. Four typical examples of such Arrhenius plots are shown in Fig. 3. It will be seen that for temperatures up to nearly 800° C, the experimental points for each specimen lie on a straight line from the slope of which an activation energy E can be determined. The decrease in (dI_{SC}/dt) preceding the onset of scattering saturation is clearly seen. The average (to the nearest kcal mole^{-1}) of the activation energies for the four synthetic quartz crystals ($W1$, $W2$, $W4$ and E-1-1) was $\bar{E} = 59 \pm 4$ kcal mole^{-1}, whereas for three amethyst quartz crystals (from batches 256 and 270) $\bar{E}$ was found to be only 36 ± 3 kcal mole^{-1}.

According to the Rayleigh scattering theory discussed above,

$R = I_{SC}/I_0 = k\sum_i N_i V_i/\lambda^4$ and hence $\log_e R = \log_e k\sum_i N_i V_i - 4\log_e\lambda$.

In order to check whether the observed scattering obeys this relation, R was measured as a function of λ at room temperature for several specimens which had previously been heated to scattering saturation. The results obtained with specimen $W2/1$ are shown in Fig. 4 and it will be seen that the experimental points lie close to a straight line of slope −4.0. For each of the other specimens examined, the slope of the straight line of best fit was in the range -4.0 ± 0.5. Thus it can be concluded that the conditions for Rayleigh scattering are reasonably well satisfied.

MBI Measurements of Volume Expansion Associated with Bubble Formation

The specimens used were $(\bar{1}\bar{1}20)$ plates, ca. 1 mm thick, cut from a block of crystal which was taken from the central Z-growth region (including the seed) of the synthetic quartz crystal $W2$. From the point of view of the variation of the hydrogen concentration which is known to occur along the [0001] direction from the seed in the Z-growth region of such crystals, all the specimens were virtually identical.

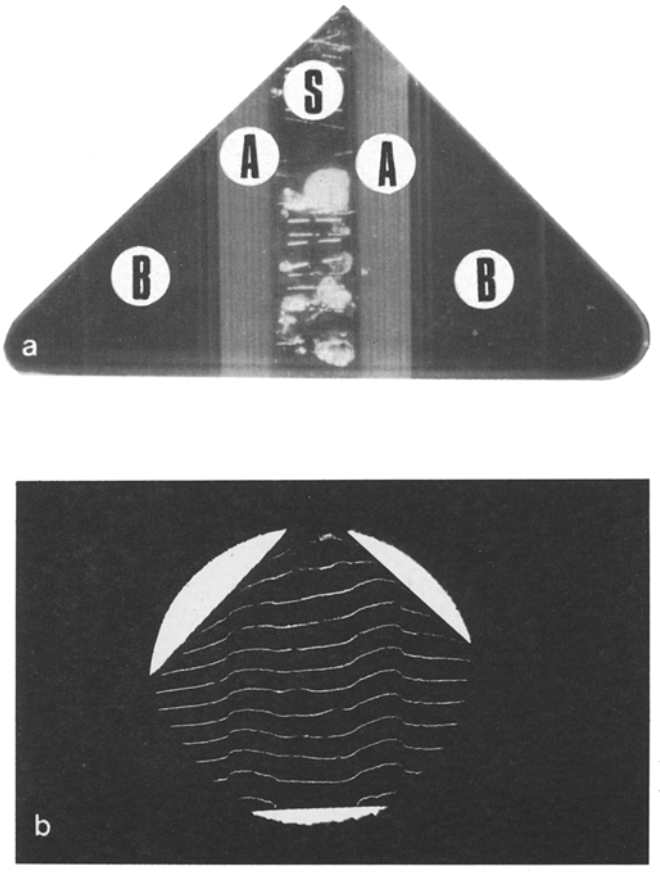

Fig. 5. a Low-power optical micrograph of one of the $(\bar{1}\bar{1}20)$ plates of crystal $W2$ used for the multiple beam interferometry and the transmission electron microscopy, after heating at 850° C to scattering saturation. The plate was illuminated from one side at approximately 90° to the axis of the microscope. Note the seed S, the bands A of intense scattering and the regions B of low scattering. The [0001] direction is horizontal. **b** Multiple beam interferogram of a crystal plate similar to that shown in **a** after heating. Note the displacement of the fringes at the boundary between each A band and the adjacent B regions, due to the relative expansion of the A bands

Figure 5a is a low-power optical micrograph of one of these specimens which had been heated at 850° C for 600 min to scattering saturation (compare Fig. 2). The specimen was illuminated from one side at approximately 90° to the axis of the microscope. The seed S (containing a number of linear fluid inclusions, some of which have burst open) is easily identified. On each side of the seed there is a band A of intense scattering about 1 mm wide. Each of these bands is composed of a number of closely-spaced narrow bands. Further away from the seed in the regions B, there is very little scattering apart from a few weaker, isolated, narrow bands. As expected, the distribution of the scattering bands is symmetrical about the seed. The hydrogen concentrations in the regions A and B were determined in an unheated specimen using the infrared technique described by Kekulawala et al. (1981) and found to be 1,400 and 800 H/10^6 Si, respectively.

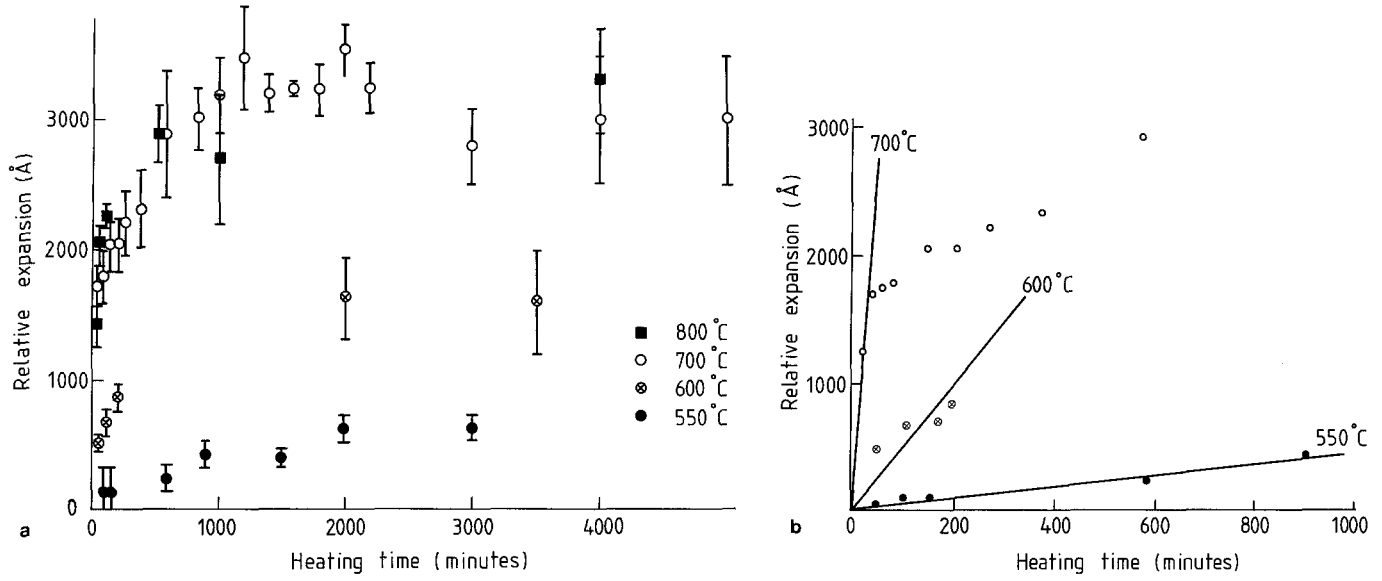

Fig. 6. **a** Graph showing the relative expansion of the A bands in $(\bar{1}\bar{1}20)$ plates of crystal *W*2 (see Fig. 5) as a function of heating time at four different temperatures. **b** The data of **a** plotted on an extended time scale for the initial 1,000 min heating time

The MBI technique was used to detect and measure any expansion (or contraction) of the crystal in the region of the band A relative to the adjacent B region, brought about by the development of the bubbles on heating. Figure 5b is a multiple beam interferogram of a heated crystal. The displacement of the fringes at the boundary between the A band and the B region (on both sides of the seed) indicates that a step has been produced. The displacement is about half a fringe spacing which corresponds to a step of height $\lambda/4 = 1{,}365$ Å. By observing the direction of the fringe displacement relative to the direction of increasing wedgegap, it was found that the band A always expanded relative to the adjacent region B. In practice, it was found that the uncertainty in the measurement of the relative expansion was usually about ± 200 Å.

In order to measure the relative expansion of A with respect to B as a function of temperature and time, the following procedure was adopted: The selected specimen was heated to a fixed temperature T_1 for a measured time t_1, then cooled to room temperature and the relative expansion α_1 measured. The same specimen was then reheated to T_1 for a period t_2, cooled to room temperature and the expansion α_2 (due to a heating time $t_1 + t_2$) measured. This procedure was repeated so that a set of measurements α_n corresponding to heating times of $t_1 + t_2 + \ldots + t_n$ was made for the temperature T_1. Such a series of experiments was carried out at temperature of 550°, 600°, 700° and 800° C, using a different specimen for each temperature. The results are plotted in Fig. 6a. It will be seen that at each temperature the relative expansion increases rapidly with time but reaches a saturation value after a heating time of about 1,000 min. The saturation value increases from about 600 Å at 550° C to about 3,400 Å at 800° C. When a crystal which had expanded to the saturation value due to heating at 550° C was subsequently heated at 800° C, it then expanded rapidly to the saturation value corresponding to the higher temperature. The relative expansions measured during the first 1,000 min for the temperatures 550°, 600° and 700° C are shown on an expanded time scale in Fig. 6b, and it is clear that for each temperature the relative expansion initially increases at an essentially constant rate which itself increases rapidly with temperature.

The rates estimated from Fig. 6b are plotted in Fig. 3b, as $\log_e(d\alpha/dt)$ against $1/T(K)$. It will be seen that the points lie on a straight line which is parallel to that obtained from the light scattering measurements, indicating the same activation energy of 56 kcal mole^{-1}. At 800° C, the initial rate of expansion was too great for any reasonable value to be estimated.

Transmission Electron Microscopy (TEM)

TEM was used to examine the microstructures which develop in amethyst and synthetic quartz due to heat-treatments similar to those given to the specimens studied by light-scattering and MBI. Specimens thin enough for TEM were prepared from 25 μm thin sections by ion-bombardment and examined in a JEM-200 A electron microscope operating at 200 kV. No features directly attributable to the ion-bombardment were observed.

Synthetic Quartz

All observations, unless otherwise stated, were made on specimens cut from the A regions of $(\bar{1}\bar{1}20)$ plates of crystal *W*2, virtually identical to that shown in Fig. 5a.

It was found that specimens taken from the B regions of unheated crystals were essentially featureless, apart from isolated areas of small (≤ 200 Å diameter) black spots, as shown in Fig. 7a. Sometimes these spots were not easily distinguishible from electron beam damage centres.

However, the A regions always exhibited features of the type shown in Fig. 7b, the density varying from about 10^{13} to 10^{14} cm^{-3}. Approximately one-third of these have a very characteristic appearance. One example is circled in Fig. 7b and it will be seen that the image consists of two sets of lobes symmetrically placed about "a line of no contrast". Ashby and Brown (1963) have shown that such an image can be due to strain around a small spherical inclusion, in which case the line of no contrast is always

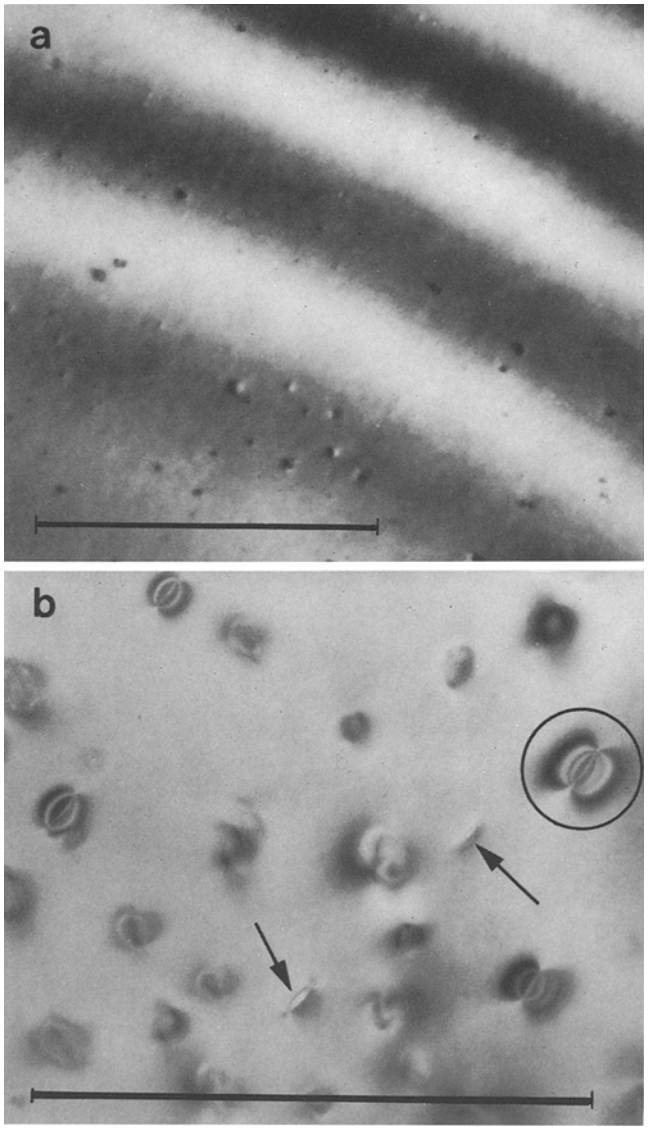

Fig. 7a, b. *Bright-field* (BF) electron micrographs of the unheated synthetic quartz, (**a**) in the B region and (**b**) in the A region of a crystal virtually identical to that shown in Fig. 5a. The scale marks indicate 1 μm

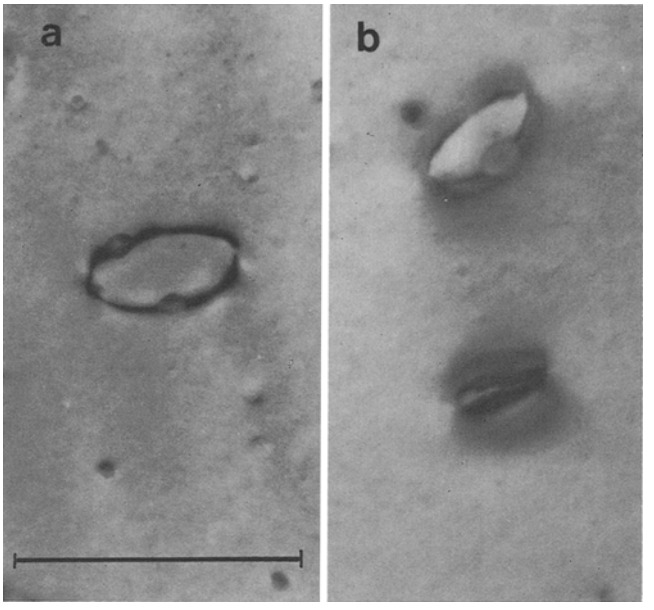

Fig. 8a, b. BF electron micrographs showing bubbles on small dislocation loops which developed after heating at 550° C for 10 min. In **b**, the lower dislocation loop appears to be developing from a strain-contrast feature of the type shown in Fig. 7b. The scale mark indicates 0.5 μm

normal to the diffraction vector **g**. However, in the present case, the line of no contrast is always parallel to [0001], independently of **g**, and this suggests that the contrast is due to strain around a small lens-shaped inclusion normal to the plane of this specimen, i.e., parallel to $(\bar{1}100)$. In addition, it was found that in *dark field* (DF) micrographs with $\mathbf{g}=(0003)$ at the exact Bragg angle ($\mathbf{s}=0$) the lobes were out of contrast and a small, black, strainfree feature was observed whose shape and orientation were consistent with the above suggestion. Morrison-Smith et al. (1976) also observed these strain features in crystal W2 and suggested that they may be due to inclusions of acmite ($NaFeSi_2O_6$). However, we were unable to detect any Na or Fe associated with these features using a transmission electron microscope fitted with energy dispersive analytical facilities. In the light of further observations, it will be suggested below that the inclusions may be water. If such an inclusion intersected the surface of the thin specimen, then the water could escape and the strain in the surrounding crystal relieved. Features which may correspond to this situation were occasionally observed. Two examples are indicated by arrows in Fig. 7b. On the basis of this model, it is also suggested that the other more common strain features seen in Fig. 7b are due to lens-shaped inclusions lying parallel to $(0\bar{1}10)$ and $(10\bar{1}0)$.

Significant changes occurred after heating at 550° C for 10 min. Distinct spherical bubbles lying on dislocation loops were now observed, as shown in Fig. 8a. The loops tend to be elongated approximately along [0001] and their longest dimension varies from about 1,000 to 10,000 Å. There are usually two or more bubbles on each dislocation loop and their diameters range from about 100 to 700 Å. There are indications that some of these loops and associated bubbles may have initiated within the strain fields of the inclusions discussed above (see Fig. 8b).

Further significant changes took place on heating at higher temperatures for longer periods. After heating at 600° C for 90 min, the density of the inclusions decreased to less than $5\times10^{12}\,cm^{-3}$, and after 200 min it was of the order of $10^{11}\,cm^{-3}$. None were observed in specimens heated for 300 and 1,000 min. Heating at 600° C also caused the dislocation loops to grow in size and the number of bubbles on each loop to increase. Typical examples in a specimen heated for 90 min are shown in Fig. 9. The closed dislocation loops have average diameters of about 7,000 Å, but it is clear that even larger dislocation loops have developed which have intersected the surfaces of the thin specimen so that only parts of the loops are actually observed. In addition, the growing dislocation loops have intersected and reacted to form three-fold nodes; this will be discussed in more detail below. The growth and interaction of the dislocation loops becomes more pronounced on heating for longer periods (e.g. 300 and 1,000 min) at 600° C, and isolated bubbles not linked by dislocations were also com-

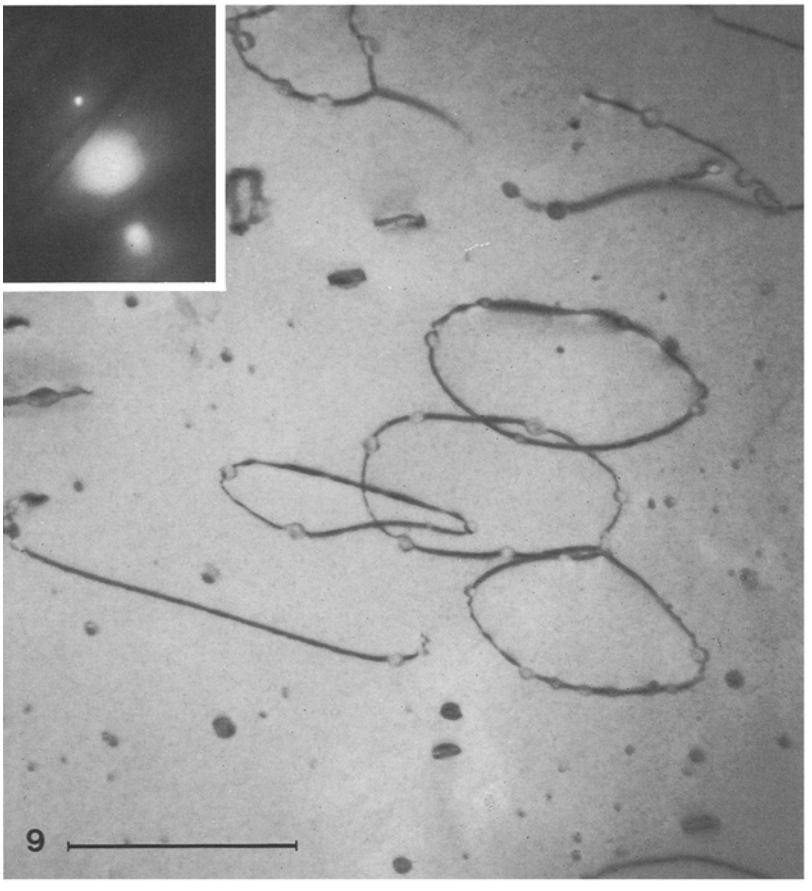

9

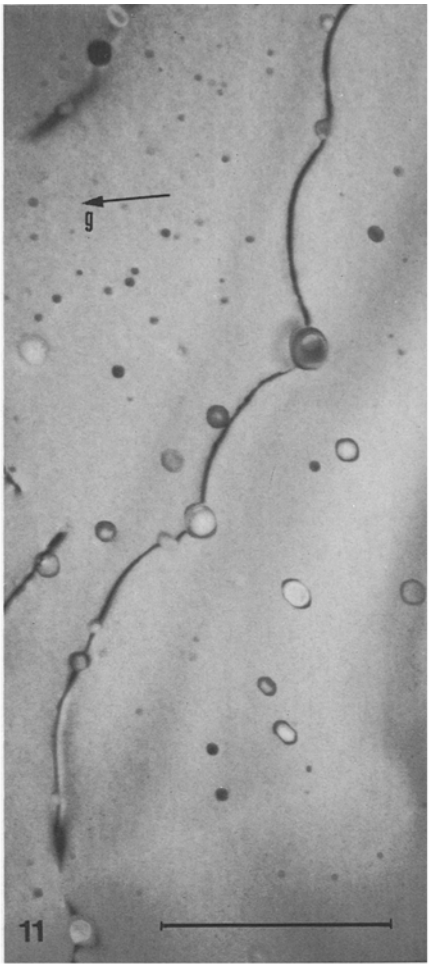

11

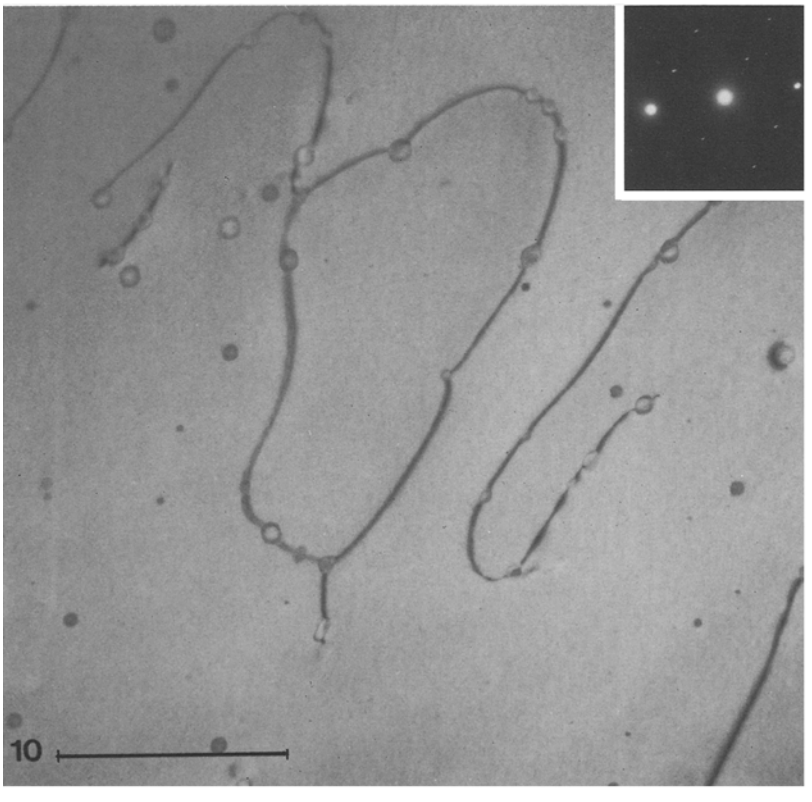

10

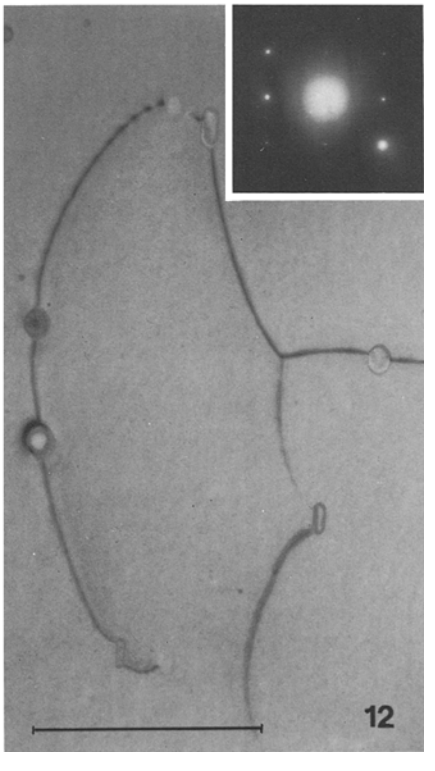

12

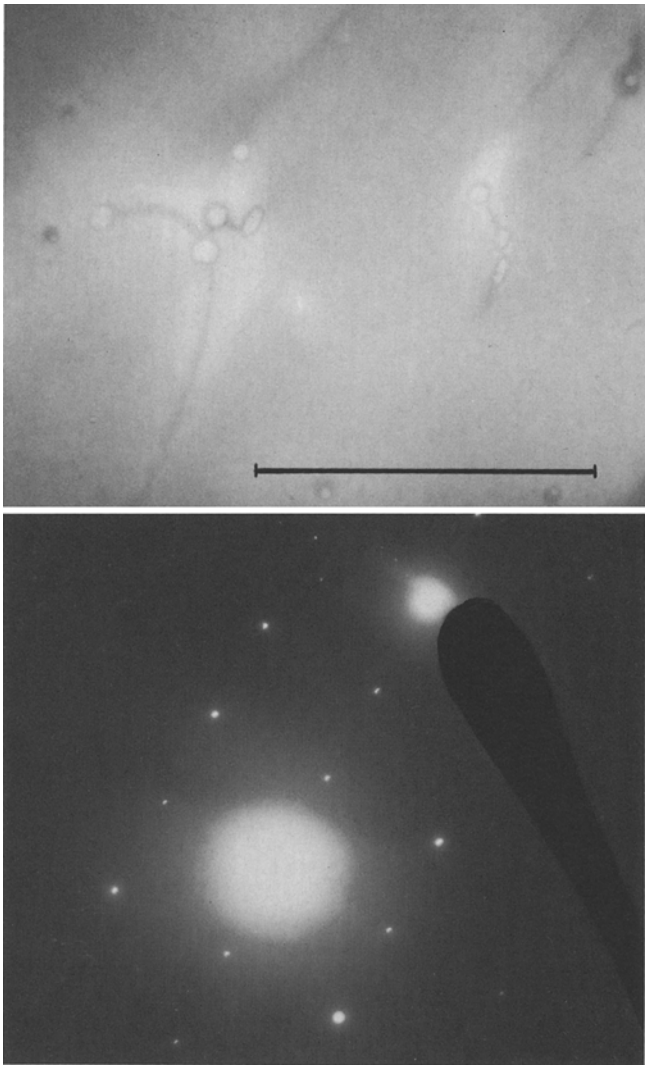

Fig. 13. *Dark-field* (DF) electron micrograph and its associated selected area electron diffraction pattern, showing that the dislocations are effectively out-of-contrast for the diffraction vector $\mathbf{g}=(0003)$. The scale mark indicates 1 μm

Fig. 9. BF electron micrograph showing bubbles on dislocation loops in a specimen heated at 600° C for 90 min. $\mathbf{g}=(\bar{1}101)$. The scale mark indicates 1 μm

Fig. 10. BF electron micrograph of a specimen heated at 600° C for 300 min. Compare with Fig. 9 and note the large loops, the isolated bubbles, and the three-fold nodes. $\mathbf{g}=(\bar{1}101)$. The scale mark indicates 1 μm

Fig. 11. BF electron micrograph of a specimen heated at 800° C for 150 min, showing a segment of a very large dislocation loop. Note the bowing-out of the dislocation between adjacent bubbles and the crystallographic shape of many of the isolated bubbles. $\mathbf{g}=(\bar{1}101)$. The scale mark indicates 1 μm

Fig. 12. BF electron micrograph of a specimen heated at 800° C for 1,000 min, showing a good example of a three-fold node. $\mathbf{g}=(\bar{1}101)$. The scale mark indicates 1 μm

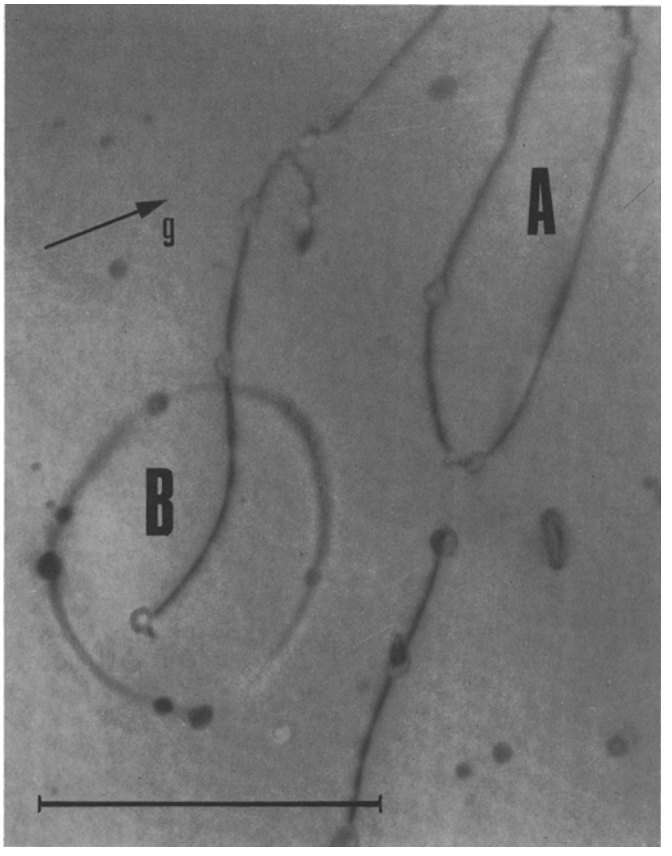

Fig. 14. BF electron micrograph showing a dislocation loop A for which $\mathbf{g}\cdot\mathbf{b}=\pm 1$ and a loop B for which $\mathbf{g}\cdot\mathbf{b}=0$, with $\mathbf{g}=(\bar{1}101)$. Specimen heated at 600° C for 90 min. The scale mark indicates 1 μm

monly observed, as shown in Fig. 10. Examination of specimens which had been heated at 800° for periods of 15, 150 and 1,000 min showed that the growth and interaction of the dislocation loops occurs more rapidly at higher temperatures. There also appears to be a significant increase in the density and size of isolated bubbles. There is no observable strain around the bubbles and many of them have become crystallographic in shape. These features are shown in Figs. 11 and 12.

Before discussing in detail the features described briefly in the previous paragraph, it will now be shown that the dislocation contrast is consistent with the loops being of edge character with $\mathbf{b}=\frac{1}{3}a<\bar{1}\bar{1}20>$. Firstly, it was found (as illustrated in Fig. 13) that the dislocations are always out-of-contrast in DF images with $\mathbf{g}=(0003)$ at $\mathbf{s}=0$. This satisfies the "effective invisibility" criterion $\mathbf{g}\cdot\mathbf{b}=0$ for $\mathbf{b}=\frac{1}{3}a<\bar{1}\bar{1}20>$.

Secondly, dislocation loops with two distinct types of image contrast are observed for all the $\mathbf{g}=\{\bar{1}101\}$ accessible in the $(\bar{1}\bar{1}20)$ sections of crystal used here. In Fig. 14, for example, it will be seen that the elongated loop A (like those in Fig. 9) appears as a single line of high contrast. On the other hand, the contrast of the near-circular loop B is distinctly different. A larger loop with the same contrast features as loop B is shown in Fig. 15. It will be seen that those parts of the loop which are approximately parallel to $\mathbf{g}$ are out-of-contrast, while those parts which are approx-

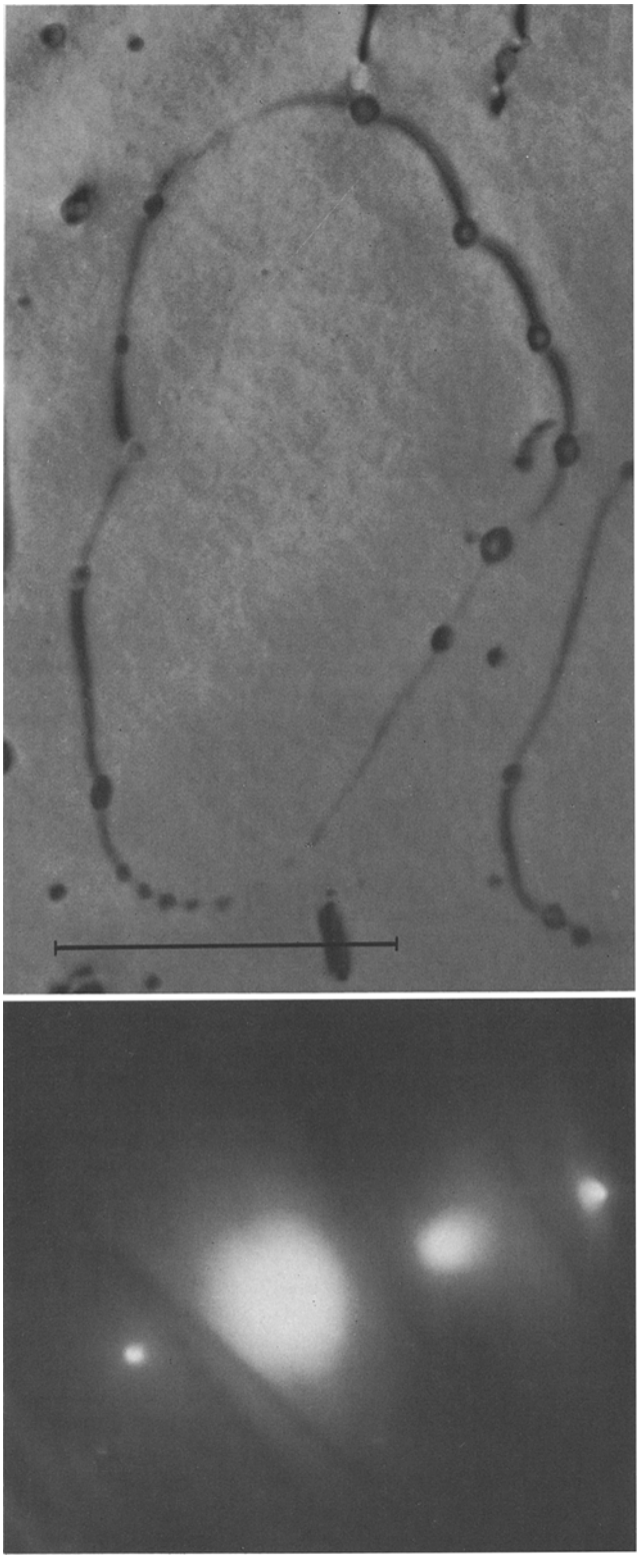

Fig. 15. BF electron micrograph of a large dislocation loop the contrast of which is characteristic of $\mathbf{g}\cdot\mathbf{b}=0$, with $\mathbf{g}=(\bar{1}101)$. Specimen heated at 600° C for 90 min. The scale mark indicates 1 μm

imately normal to **g** exhibit a double image. Eddington (1975) has shown that these contrast features are characteristic of edge dislocation loops with $\mathbf{g}\cdot\mathbf{b}=0$ in an elastically isotropic medium. Since these loops are clearly lying in the plane of the specimen $(\bar{1}\bar{1}20)$, which is an elastic symmetry

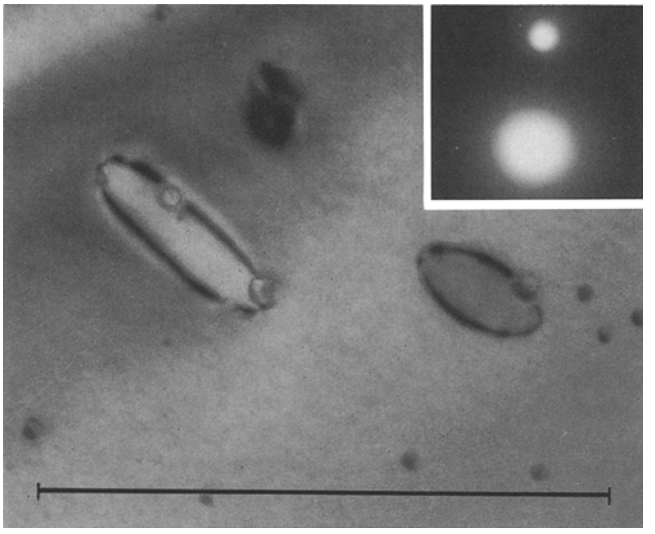

Fig. 16. BF electron micrograph showing a change of background contrast between the inside and outside of two edge dislocation loops. The fact that the contrast-change for one loop is in the opposite sense from the other loop suggests that one lies in $(2\bar{1}\bar{1}0)$ and the other in $(\bar{1}2\bar{1}0)$. $\mathbf{g}=(\bar{1}101)$. Specimen heated at 550° C for 10 min. The scale mark indicates 1 μm

plane for quartz (Retchford 1973), isotropic elasticity theory applies. Thus the observed contrast of these loops is consistent with $\mathbf{b}_3=\frac{1}{3}a[\bar{1}\bar{1}20]$, which is normal to the plane of the loop.

For the other crystallographically equivalent burgers vectors $\mathbf{b}_1=\frac{1}{3}a[2\bar{1}\bar{1}0]$ and $\mathbf{b}_2=\frac{1}{3}a[\bar{1}2\bar{1}0]$, $\mathbf{g}\cdot\mathbf{b}=\pm 1$ for all the $\mathbf{g}=\{\bar{1}101\}$ accessible in these sections. Edge dislocation loops with these burgers vectors will lie in the $(2\bar{1}\bar{1}0)$ and $(\bar{1}2\bar{1}0)$ planes, both of which are inclined at 60° to the $(\bar{1}\bar{1}20)$ plane of the crystal specimen; further, they will exhibit the *same* strong contrast. Thus, if the loops are approximately circular, they will appear elongated parallel to [0001]. These features are characteristic of loops of the type shown in Fig. 9. Another contrast feature which is consistent with this interpretation is shown in Fig. 16: the observed change of background intensity from the outside to the inside of the loop indicates that diametrically opposite sides of the loop are of opposite sign, as required for a loop of edge character. Therefore, the features of all the dislocation loops observed are consistent with their being edge in character with $\mathbf{b}=\frac{1}{3}a<\bar{1}\bar{1}20>$.

Since the dislocation loops are associated with the bubbles (which must be considered as Si and O vacancy clusters) and since the growth of the loops is correlated with expansion of the crystal, it is probable that the loops are *interstitial* in character. Further evidence for this conclusion will be given below.

Having established the character of the dislocation loops, it is clear that they grow in size by climb. If the bubbles are not carried along at the same speed as the climbing dislocation, then the segment of a dislocation loop between two such bubbles will bow out, and is often observed – see Figs. 11 and 15, for example. It is possible that a climbing dislocation may break away from a relatively large bubble, leaving it isolated.

If two expanding loops intersect, then the resulting dislocation arrangement will depend upon the burgers vectors of the loops. Consider two such loops, shown diagrammati-

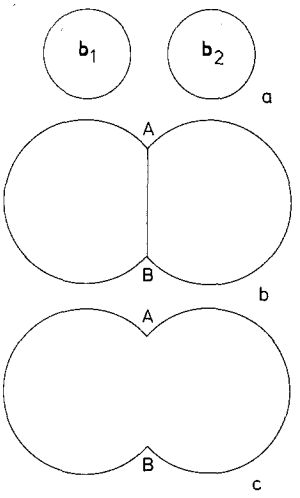

Fig. 17a–c. Schematic diagrams illustrating the intersection of the two edge dislocation loops shown in **a**. In **b**, $\mathbf{b}_1 \neq \mathbf{b}_2$ and the common segment AB has a burgers vector $\mathbf{b}_1 + \mathbf{b}_2 = -\mathbf{b}_3$. In **c**, $\mathbf{b}_1 = \mathbf{b}_2$ and the intersecting segments between A and B annihilate each other

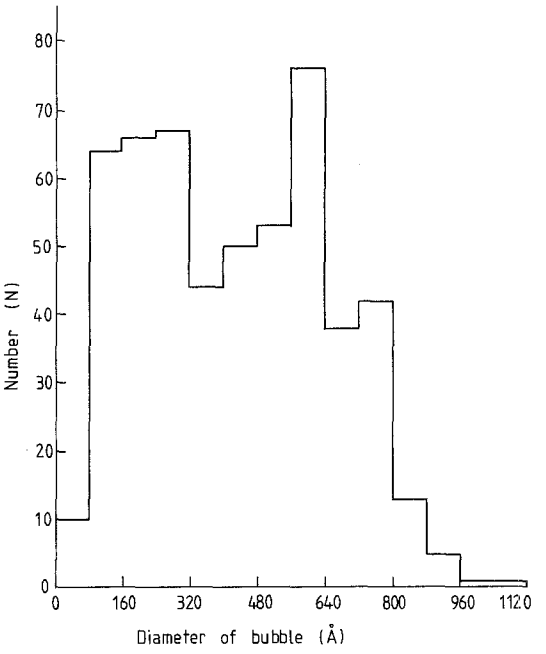

Fig. 18. Frequency distribution of bubble size determined from a set of random micrographs of a specimen which had been heated at 850° C to scattering saturation

cally in Fig. 17a. If $\mathbf{b}_1 \neq \mathbf{b}_2$ then the situation after intersection will be as shown in Fig. 17b, and it is clear that the segment of dislocation AB which is common to both loops will have a burgers vector $\mathbf{b}_1 + \mathbf{b}_2 = -\mathbf{b}_3$. Examples of threefold nodes probably formed in this way are shown in Figs. 9, 10 and 12. It will be noted that in each case two of the dislocations are in strong contrast (corresponding to $\mathbf{g}\cdot\mathbf{b} = \pm 1$) while the contrast of the third dislocation is characteristic of $\mathbf{g}\cdot\mathbf{b} = 0$. Frequently, a bubble is present at the nodes, as shown in Fig. 10. On the other hand, if $\mathbf{b}_1 = \mathbf{b}_2$, then the situation after intersection will be as shown in Fig. 17c. It is clear that the intersecting segments between A and B will annihilate each other and a single large loop will be formed. Continuing climb will remove the cusps at A and B, unless they are pinned by bubbles. The shape of the large loop in Fig. 15 suggests that it may have formed in this way. If there were a bubble (no matter what size) on either of the intersecting segments between A and B then it will be left isolated after the intersection has taken place. This is a more likely mechanism for producing isolated bubbles than the one previously suggested.

Finally, the distribution of bubble sizes was measured from a series of 33 random electron micrographs of a thin specimen cut from a block of crystal W2 which had been heated at 850° C to scattering saturation. The resulting histogram (Fig. 18) appears to be slightly bimodal, as found previously by Kekulawala et al. (1981). The total volume of specimen examined was 50 μm^3, assuming a thickness of 0.3 μm. The number density and volume fraction of bubbles were found to be 10^{13} cm^{-3} and 4×10^{-3}, respectively.

Two deductions can be made from this value of the volume fraction of bubbles:

Firstly, if the volume of the crystal increases due to the formation of the bubbles, then the linear expansion will be given by

$$\Delta l/l = \tfrac{1}{3}(4 \times 10^{-3}).$$

Thus, the expected height of the step formed on *each* surface of the 1 mm thick crystal shown in Fig. 5a after heating to expansion saturation at 850° C will be $\Delta l/2 = (4 \times 10^{-3})(l/6) = 6{,}667$ Å. In this calculation, it has been assumed that only region A will expand. Since this is clearly not the case, the calculated value must be an over-estimate. However, in view of the uncertainty in the value of the volume fraction of bubbles, it is in reasonable agreement with the height of the step measured by the MBI technique after heating to saturation at 800° C (see Fig. 6a).

Secondly, if it is assumed that all the hydrogen in the crystal is converted to H_2O at NTP in the bubbles, then the average filling factor is found to be 14 percent for the hydrogen concentration of 1,400 H/10^6 Si measured by infrared absorption in the A region of the crystal shown in Fig. 5a.

Amethyst Quartz

A limited number of observations were made on specimens of amethyst quartz which had been heated at 550° to 600° C for a period of from 15 to 60 min in order to see whether the early stages of bubble formation were similar to those observed in the synthetic quartz.

Figure 19a shows a set of the ubiquitous Brazil twin boundaries on major rhombohedral planes, viewed edge-on. As in all specimens examined, the boundaries are decorated with very small precipitates but their nature is not known. On heating at 550° C for 15 min, strain contrast features (similar to those observed in unheated synthetic quartz, Fig. 7b) developed along the twin boundaries and, very occasionally, in isolation. These features were still present after heating at 600° C for 60 min, as shown in Fig. 19b. However, they were never observed in specimens heated at ca. 800° C to scattering saturation which exhibited a high density of bubbles along the twin boundaries (see McLaren and Phakey 1966a).

Figure 19c shows an example of a dislocation loop with bubbles which has grown out from a twin boundary at a position where a strain-contrast feature is also observed.

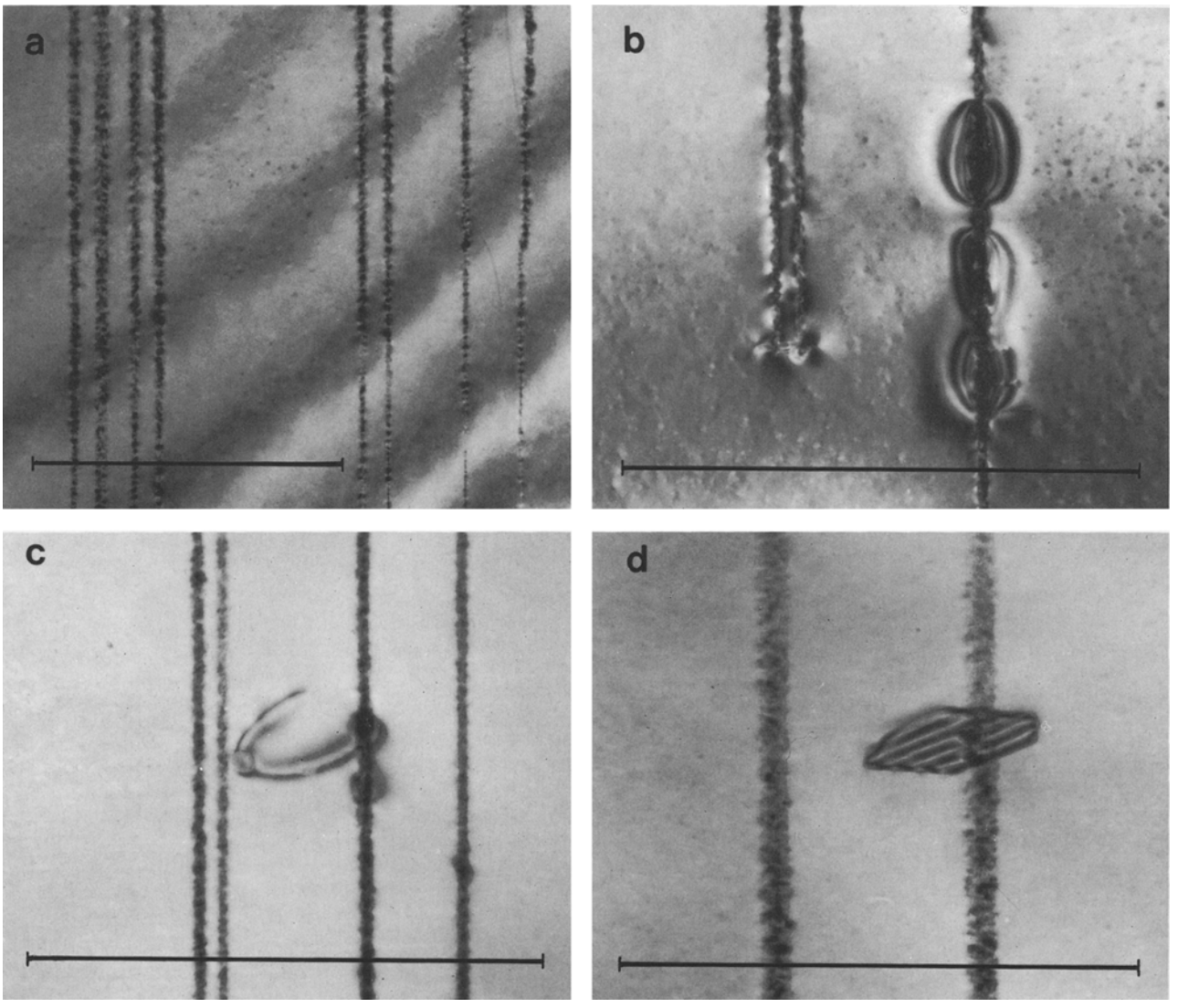

Fig. 19a–d. Set of BF electron micrographs of amethyst quartz. **a** Unheated crystal showing decorated Brazil twin boundaries viewed edge-on. **b** Strain-contrast features, similar to those in unheated synthetic quartz (Fig. 7b), observed in a specimen heated at 600° C for 60 min. **c** Bubbles on a dislocation loop which appears to have developed from a Brazil twin boundary on heating at 550° C for 20 min. **d** A faulted dislocation loop which has developed from a very narrow Brazil twin lamella in the same specimen as **c**. The scale marks indicate 1 μm

The diffraction-contrast "shadow" within the loop is evidence of its edge character.

Not infrequently, faulted loops were observed as shown in Fig. 19d. However, in all examples observed, the loop developed from a very thin twin lamella and not from a single twin boundary. It is clear that if an *interstitial* loop were initiated within a thin twin lamella and grew beyond it, then the interstitial layer within the loop would be in twin orientation with respect to the crystal around it. The fringes within the loop are characteristic of overlapping Brazil twin boundaries when $\alpha = 2\pi \mathbf{g} \cdot \mathbf{R} \neq 180°$ (see McLaren and Phakey 1966b; McLaren et al. 1967). It will be noted that the loop in Fig. 19d also appears to be associated with one of the strain-contrast features of the type shown in Fig. 19b. The observation of these faulted loops is considered to be further evidence in support of the earlier suggestion that the edge dislocation loops associated with the bubbles in both synthetic and amethyst quartz are interstitial in character.

Discussion

In this section a mechanism for the formation of the bubbles will be proposed. Since this mechanism is based on a new model for the incorporation of hydrogen in quartz, the previously suggested model of Brunner et al. (1961) will be discussed first, together with the reasons for rejecting it in favour of the new model which will be developed in detail. Then, after having formulated the mechanism of bubble formation, the experimental observations of the rate of bubble formation as a function of temperature will be used to provide kinetic data on hydrogen and self-diffusion in quartz. Finally, the relevance of these observations to hydrolytic weakening will be mentioned briefly.

Models for the Incorporation of Hydrogen in Quartz

As already discussed in the Introduction, it is the hydrogen associated with the broad, isotropic infrared absorption

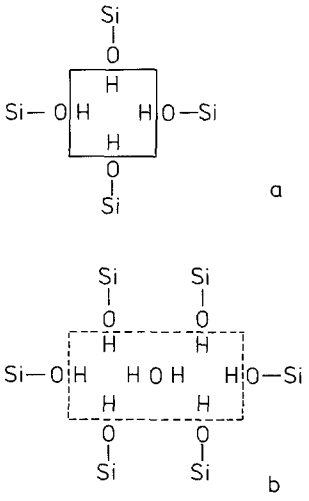

Fig. 20. **a** Schematic diagram of a Si vacancy occupied by 4 H. **b** Schematic diagram of an adjacent pair of the defects shown in **a**

band extending from ca. 3,700 cm^{-1} to 2,600 cm^{-1} which appears to be involved in the development of bubbles. Brunner et al. (1961) proposed that H_2O could be incorporated in quartz by hydrolysing silicon-oxygen bridges:

$$Si-O-Si+H_2O \rightarrow Si-OH\cdot HO-Si.$$

This model seems unlikely for two reasons: Firstly, there is no direct evidence to suggest that it would produce a broad, isotropic infrared absorption band. On the contrary, the bonding of the hydrogen suggests that it may produce relatively sharp absorption peaks. Secondly, the model is probably not possible *structurally*. Recent work by O'Keeffe and Hyde (1978) on Si–O–Si configurations in silicates suggests that the size of the Si atoms is such that adjacent SiO_4 tetrahedra are in contact and that there is probably no space to accommodate an extra O and 2 H in a normal Si–O–Si linkage.

More recently, Nuttall and Weil (1980) in their low temperature (ca. 25 K) electron paramagnetic resonance studies of single crystals of synthetic quartz, which had been X-irradiated, revealed the presence of two new trapped-hole impurity centres. The first is formed by the trapping of an electron hole at an oxygen ion adjacent to a Si vacancy occupied by 4 H; the second is similar with only 3 H present. On the basis of these observations they proposed that, before irradiation, 4 H are associated with a Si vacancy to preserve local charge neutrality. This model is shown schematically in Fig. 20a. It will be referred to as the $(4\ H)_{Si}$ defect.

There are a number of reasons for preferring this hydrogen defect centre over the one previously suggested by Brunner et al. (1961). It is structurally feasible and it can, presumably, diffuse in the same way as a Si vacancy. Perhaps its most important property in the present context is that an adjacent pair of $(4\ H)_{Si}$ defects produces an elemental water bubble, as shown in Fig. 20b, in its own space. Furthermore, larger bubbles can, in principle, be produced simply by clustering of the defects, n of them producing a bubble of $(n\text{-}1)H_2O$. However, since such bubbles create their own space, they cannot produce directly any expansion of the crystal. There are indications, not yet fully investigated, that the forces between the hydrogens in a $(4\ H)_{Si}$ defect are slightly repulsive and that these forces are relaxed in a defect pair. Thus, the clustering of the $(4\ H)_{Si}$ defects is energetically favourable.

A random distribution of isolated $(4\ H)_{Si}$ defects may or may not produce a broad isotropic infrared absorption band, but it is highly probable that such an absorption band would be produced if a large number of defect-pairs existed. The absorption would be isotropic because of the several possible pair directions in the structure, and the band would be broad due to the two sets of OH bonds in the defects – one set associated with the O bonded to Si, and the other associated with the H_2O. Exchange of H between the sets is likely to broaden the band further. The presence of H_2O in the defect-pair suggests that the absorption may be not unlike that of molecular water, and this should become more apparent for larger clusters of $(4\ H)_{Si}$ defects. Another important property of these defects is that they can in principle be created if water is forced into a quartz crystal, as shown by the following reaction:

$$n(SiO_2)+2H_2O \rightarrow [(4H)_{Si}O_2+(n-1)SiO_2]_{internal} + [SiO_2]_{surface}.$$

Mechanism of Bubble Formation and Growth

It is assumed initially that hydrogen is incorporated by means of $(4\ H)_{Si}$ defects. Although the distribution is unknown, it seems likely that the defects occur in isolation ($n=1$), as pairs ($n=2$) and perhaps in larger clusters ($n \geqq 3$). At temperatures of ca. 550° C and above, the single $(4\ H)_{Si}$ defects begin to diffuse and, as a result, new pairs will form and larger clusters will grow.

Suppose now that a spherical cluster of $3n$ $(4\ H)_{Si}$ defects exists in the crystal. This would have a volume V_b equal to that of n unit cells, i.e. $112\,n$Å^3, and a diameter $d=6n^{1/3}$ Å. It would contain $(3n-1)H_2O$ which would occupy a volume $V_w=30(3n-1)$Å^3 at NTP. Thus, for a water bubble so formed, the volume fraction of water is $30(3n-1)/112n$ which is about 80 percent for all $n \geqq 10$, corresponding to a specific volume V_s ($=1$/volume fraction) of 1.25. From the curves of "steam" pressure P(kbar) as a function of temperature (T° C) given in Fig. 21, it will be seen that the pressure in the bubble will be 7.5 kbar at 800° C, for example. A pressure of this magnitude would be expected to cause the surrounding crystal to fracture or to deform plastically. However, the TEM observations have shown that the bubbles which develop on heating are strain-free. Furthermore, it has been shown that the crystals expand due to the formation of the bubbles and calculations indicate that the specific volume V_s of the water in these bubbles may be as high as 7.1, corresponding to a filling factor of only 14 percent. These observations indicate that the stress around a cluster of $3n(4\ H)_{Si}$ defects is relaxed (without fracture or plastic deformation) by the bubble becoming larger, thus increasing V_s and decreasing the pressure P. The mechanism by which this increase in volume occurs will be discussed later.

The question now arises as to what limits the growth of the bubble – to what value must P be reduced? In the absence of any other information, it is suggested that the volume V_b of the bubble increases until P is reduced to a value equal to the pressure difference p across the surface of a spherical bubble in mechanical equilibrium. This is given by

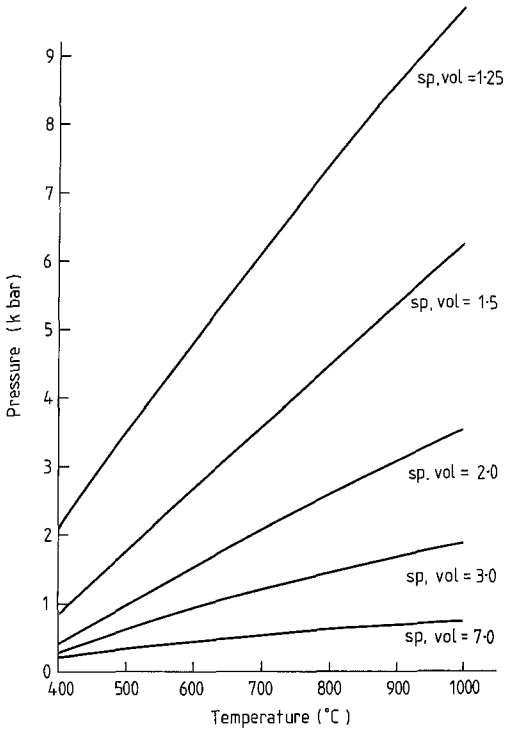

Fig. 21. Curves of the "steam" pressure P as a function of temperature for a number of values of the specific volume. Data obtained from the tables of Burnham et al. (1969)

$$p=\frac{4\gamma}{d} \tag{8}$$

where γ is the surface energy. Of course this can be achieved only if $P>p$ and if P decreases more rapidly than p with increasing d . From the curves of Fig. 21 it is found that the variation of P with V_s at any temperature T, is reasonably well described by the expression

$$PV_s^2=\text{constant} \tag{9}$$

over the range $1.25<V_s<3.0$. Now, assuming the mass of water in the bubble does not change, V_s is proportional to V_b and by comparing Eqs. (8) and (9) it is clear that P decreases very much more rapidly than p with increasing d. In order to determine p, at least an estimate of the value of γ must be known.

The surface energies of a number of common ceramics have been estimated by Bruce (1965) from measurements of the sublimation energy. For β-cristobalite, the surface energy γ_a (averaged over all crystallographic planes) was found to be $0.766\ \mathrm{Jm}^{-2}$ at 550° C and $0.708\ \mathrm{Jm}^{-2}$ at 850° C. Bruce suggests that since α-quartz has a higher density, it will have a higher value of γ_a, perhaps $1\ \mathrm{Jm}^{-2}$. However, he also points out that γ_a is significantly reduced by the adsorption of a fluid. For example, the value for mica in air is about one-third the value in vacuum. Thus for a quartz surface wetted with water in which it is slightly soluble, γ_a may be similar to that of fused quartz. Bruce quotes a value of $\gamma_a=0.290\ \mathrm{Jm}^{-2}$ measured on a fused quartz fibre at 1,100° C, while the heat of solution of amorphous SiO_2 gave $\gamma=0.259\ \mathrm{Jm}^{-2}$ at 23° C. In view of these measurements a value of $\gamma_a=0.3\ \mathrm{Jm}^{-2}$ is perhaps a reasonable value to assume in the discussion of water bubbles in quartz at temperatures in the range 550° to 850° C. Thus Eq. (8) becomes

$$p(\text{kbar})=\frac{120}{d(\text{Å})} \tag{10}$$

As an example, consider a cluster or bubble of $300(4\ \mathrm{H})_{\mathrm{Si}}$ defects for which $d=28$ Å and, from Eq. (10), $p=4.3$ kbar. The specific volume $V_s=1.25$ and at 800° C the water pressure $P=7.5$ kbar, from Fig. 21. Therefore, at this temperature, the bubble will grow without trapping any more $(4\ \mathrm{H})_{\mathrm{Si}}$ defects. Bubbles of this initial diameter are expected to grow at all temperatures down to 550° C where $P=p=$ 4.3 kbar. Clearly, the minimum diameter d_m of a bubble which will just grow will decrease with increasing temperature. At 800° C, for example, $d_m=16$ Å. From Fig. 18 it will be seen that for specimens heated to saturation at 850° C, the mean bubble diameter is about 480 Å and it has also been shown that the filling factor for such bubbles is about 14% (corresponding to $V_s=7.1$). Thus from Eq. (10), $p=0.25$ kbar and from Fig. 21, $P=0.5$ kbar. The values are not inconsistent with the suggestion that the bubbles grow until P and p become equal.

If a cluster of $(4\ \mathrm{H})_{\mathrm{Si}}$ defects is formed at some temperature $T_1>$ ca. 550° C, and the crystal then cooled fairly rapidly to $T_2<550$° C, it is possible that the cluster would be frozen-in before it had time to grow. It is suggested that this is the origin of the precipitates which give rise to the strain-contrast features observed in the amethyst quartz after heating for short periods at temperatures from 550° to 600° C. The similar features observed in the synthetic quartz may have formed in the final cooling stages after the crystal had grown. It is significant that these features are larger and more common in the regions of relatively higher hydrogen concentration in synthetic quartz and along the twin boundaries in amethyst. Further, they are not observed in crystals heated above ca. 600° C, and there are indications, at low temperatures, that bubbles and associated dislocation loops are generated in their neighbourhood.

The mechanism by which the bubbles grow is indicated by the TEM observations. It has been shown that the bubbles grow in association with edge dislocation loops of $\mathbf{b}=\frac{1}{3}a<\bar{1}\bar{1}20>$. It is clear that if a bubble is to grow without an increase in the number of $(4\ \mathrm{H})_{\mathrm{Si}}$ defects, then Si and O must be removed from the bubble site. The TEM observations indicate that these atoms form the edge dislocation loops which must therefore be interstitial in character. Since the bubbles lie on the dislocation loops, the diffusion of the Si and O from the bubble to the loop must take place by pipe diffusion along the dislocation. If this is the mechanism by which both the bubbles and the dislocation loops grow, then it would be expected that the total volume of the bubbles ΣV_b on a dislocation loop would be equal to $A|\mathbf{a}|$, where A is the area of the loop, plus the volume of the trapped $(4\ \mathrm{H})_{\mathrm{Si}}$ defects which is probably less than 20% of ΣV_b. From seven of the closed loops shown in Figs. 8a, 9, 14–16, it was found that ΣV_b and $A|\mathbf{a}|$ for each loop never differed by more than a factor of 3. In view of the error involved in measuring the diameter of the bubbles (which was usually about 200 Å), this result is not inconsistent with the proposed mechanism.

As already pointed out, the clustering of $(4\ \mathrm{H})_{\mathrm{Si}}$ defects cannot of itself produce any expansion of the crystal. In fact, it is the growth of the interstitial edge dislocation loops which is directly responsible for the observed expansion.

It is clear that at any temperature $T\geqq 550$° C, a bubble

will grow (a) by the trapping of diffusing $(4\ H)_{Si}$ defects which will increase $(P-p)$ and (b) by diffusion of Si and O away from the bubble into the associated interstitial edge dislocation loop which will decrease $(P-p)$ to zero. These two processes will take place virtually simultaneously, and the bubbles will continue to grow until all the available $(4\ H)_{Si}$ defects have been trapped. This situation is manifested by the eventual saturation with heating time of the intensity of the light scattering and the expansion, as shown in Fig. 2 and Fig. 6a, respectively. Also, the higher the temperature at which the bubbles are formed, the higher will be the pressure developed in the bubbles and therefore, on the average, the bubbles will grow larger by expanding the dislocation loops. Thus, the magnitude of the expansion at saturation will increase with increase in temperature, as is observed in Fig. 6a.

Diffusion Kinetics

Since the light scattering and the volume expansion are simply different manifestations of the same phenomenon, the activation energies determined from the two types of experiment should be the same for any given crystal. This is shown to be so for crystal *W2* in Fig. 3b. It was also found that for all the synthetic quartz crystals studied the activation energy E was about 60 kcal mole^{-1}, but for amethyst it was only about 36 kcal mole^{-1}.

The proposed mechanism of bubble formation involves two diffusion processes: (a) the diffusion of $(4\ H)_{Si}$ into the bubble and (b) the diffusion of Si and O away from the bubble directly into the linked interstitial edge dislocation loop. There is no direct information to indicate which is the slower of the two processes. Process (a) is similar to Si self-diffusion by a vacancy mechanism and process (b) is similar to pipe diffusion along a dislocation core. Intuitively, one would expect process (a) to be the slower. If it is assumed that the *same* process is the slower in both amethyst and synthetic quartz, then in order to determine the rate-determining process it is necessary to find which of the two possible processes (a) and (b) is the more likely to give rise to the different activation energies observed in the two materials. Although it seems unlikely that type (b) diffusion will be different, this may not be true of the diffusion of $(4\ H)_{Si}$ defects. In synthetic quartz these defects diffuse in random directions, but in amethyst (since there is evidence that the hydrogen is concentrated locally in the Brazil twin boundaries where the bubbles form preferentially) the $(4\ H)_{Si}$ defects may diffuse preferentially in the twin boundaries with a lower activation energy. In addition, it is perhaps possible that the presence of a relatively high concentration of Fe^{3+} ions in amethyst (McLaren and Pitkethly 1982) may also influence the diffusion of species such as the $(4\ H)_{Si}$ defects.

An estimate of the value of the diffusion constant D for the $(4\ H)_{Si}$ defects in synthetic quartz can be obtained from the TEM observations using the analysis of the kinetics of precipitation given by Shewmon (1963). He has shown that if the precipitate particles are randomly distributed then it is possible to treat the specimen as a close-packed collection of spherical cells of radius r_e (each containing one precipitate particle) across the boundaries of which there is no net flux. Thus diffusion in one cell only need be considered. Assuming the precipitate to be a sphere of radius $\alpha \ll r_e$ then, for the initial period of precipitation, it follows that the rate of change of the average concentration $\bar{C}$ of the solute in solution is given by

$$\frac{d\bar{C}}{dt} = \frac{3D}{r_e^3}(C_0 - C')\,\alpha(t) \tag{11}$$

where $\bar{C} = C_0$ at $r = r_e$ and $\bar{C} = C'$ at $r = \alpha$.

In applying Eq. (11) to the present problem we put $d\bar{C}/dt = C_0/t_0$ where t_0 is the time taken for all the hydrogen in the crystal to be precipitated as water in the bubbles at any given temperature T – this can be estimated from Fig. 6a. We also put $C' = O$. Thus Eq. (11) becomes

$$D = r_e^3/3\,t_0\alpha. \tag{12}$$

An estimate of r_e can be obtained from the electron micrographs if it is assumed that $r_e = (1/2)\bar{d}$, where $\bar{d}$ is the average distance between bubbles. If we take $r_e = 0.25$ μm, $\alpha = 240$ Å and $t_0 = 1{,}000$ min then $D = 3.6 \times 10^{-14}$ cm^2 s^{-1}. It is clear that r_e is the most difficult of these parameters to estimate and also the one which most influences the calculated value of D. For example, if $r_e = 0.1$ μm then $D = 2.3 \times 10^{-15}$ cm^2 s^{-1}.

If the $(4\ H)_{Si}$ defects diffuse like Si vacancies, then the activation energies and diffusion constants may also be similar. Giletti et al. (1976) measured the diffusion of ^{30}Si in natural quartz over the temperature range 912° to 1,028° C and found an activation energy of 55 kcal mole^{-1}. However, the diffusion constant D was about 2×10^{-18} cm^2 s^{-1} (extrapolated to 727° C). The estimate of $D \approx 10^{-14}$ cm^2 s^{-1} is similar to the value measured by Giletti and Yund (1982) for the self-diffusion of oxygen in quartz under hydrothermal conditions at 727° C. However, the activation energy was only 40 kcal mole^{-1}. Thus no general conclusions can be drawn from these comparisons.

Conclusions and Application to Hydrolytic Weakening

The mechanisms which have been proposed for the formation and growth of strain-free water bubbles and associated dislocations in heat-treated synthetic quartz may be summarized as follows:

(1) It is assumed that hydrogen is incorporated in the quartz structure by means of $(4\ H)_{Si}$ defects.

(2) On heating, these defects diffuse and clusters develop. A cluster of $n(4\ H)_{Si}$ defects produces a water bubble containing $(n\text{-}1)\ H_2O$, without any increase in the volume of the crystal.

(3) For all $n \geqq 10$, the specific volume of water in such a bubble is $V_s = 1.25$, corresponding to 80 percent full. At any temperature T there is a critical bubble diameter d_m (which decreases with increasing T) above which the "steam" pressure P exceeds the pressure p for a spherical bubble in mechanical equilibrium.

(4) If P becomes greater than p, then the bubble increases in volume until $P = p$, the increase in volume being achieved by the pipe diffusion of Si and O away from the bubble site into a linked dislocation loop of $\mathbf{b} = \frac{1}{3}a\langle\bar{1}\bar{1}20\rangle$. This process produces the observed increase in volume of the specimen.

(5) At any fixed temperature T, the diffusion processes (2) and (4) take place virtually simultaneously and continue until all the $(4\ H)_{Si}$ defects have been trapped in the bubbles.

(6) The growth and interaction of the dislocation loops

provide mechanisms for isolating bubbles from the dislocations.

(7) Arguments are presented which suggest that the diffusion of the $(4\ H)_{Si}$ defects is the rate determining process and values of the activation energy and the diffusion constant are deduced.

Perhaps the most important aspect of this work is that it appears to establish the $(4\ H)_{Si}$ defect as the "hydroxyl species" responsible for the hydrolytic weakening of quartz. If this is so, then it is now necessary to investigate how these defects interact with, and influence the glide and climb of, the dislocations involved in the deformation process.

Acknowledgements. We thank the ARGC for generous financial support, and M.S. Paterson, B.G. Hyde and R.A. Yund for many stimulating discussions.

References

Ashby MF, Brown LM (1963) Diffraction contrast from spherically symmetrical coherency strains. Philos Mag 8:1083–1103

Bambauer HU, Brunner GO, Laves F (1963) Merkmale des OH-Spektrums alpiner Quartz (3 Micron-Gebiet). Schweiz Mineral Petrogr Mitt 43:259–268

Bruce RH (1965) Aspects of the surface energy of ceramics. I. Calculations of surface free energies. In: Stewart GH (ed) Science of ceramics, Vol 2. Academic Press, London New York, pp 359–367

Brunner GO, Wondratschek H, Laves F (1961) Ultrarotuntersuchungen über den Einbau von H in natürlichen Quarzen. Z Elektrochem 65:735–750

Burnham CW, Holloway JR, Davis NF (1969) Thermodynamic properties of water to 1,000° C and 10,000 bars. Geol Soc of America, Special Paper Number 132

Dodd DM, Fraser DB (1965) The 3,000–3,900 cm^{-1} absorption bands and anelasticity in crystalline quartz. J Phys Chem Solids 26:673–686

Eddington JW (1975) Monographs in practical electron microscopy in materials science. 3 Interpretation of transmission electron micrographs. NV Philips' Gloeilampenfrabrieben, Eindhoven

Giletti BJ, Yund RA, Semet M (1976) Silicon diffusion in quartz. Geol Soc Am Abstr Progr 8:883–884

Giletti BJ, Yund RA (1982) Self-diffusion of oxygen in quartz. Eos (in press)

Griggs DT, Blacic JD (1965) Quartz: Anomalous weakness of synthetic crystals. Science 147:292–295

Hobbs BE, McLaren AC, Paterson MS (1972) Plasticity of single crystals of synthetic quartz. In: Geophysical monograph Vol 16:Flow and fracture of rocks. American Geophysical Union, pp 29–53

Kats A (1962) Hydrogen in alpha-quartz. Philips Res Rep 17:133–279

Kekulawala KRSS, Paterson MS, Boland JN (1981) An experimental study of the role of water in quartz deformation. In: Geophysical monograph Vol 24: Mechanical behaviour of crustal rocks. American Geophysical Union, pp 49–60

Kerker M (1969) The scattering of light. Academic Press, New York London

McLaren AC, Phakey PP (1966a) Transmission electron microscope study of bubbles and dislocations in amethyst and citrine quartz. Aust J Phys 19:19–24

McLaren AC, Phakey PP (1966b) Electron microscope study of Brazil twin boundaries in amethyst quartz. Phys Status Solidi 13:413–422

McLaren AC, Pitkethly DR (1982) The twinning microstructure and growth of amethyst quartz. Phys Chem Minerals 8:128–135

McLaren AC, Retchford JA, Griggs DT, Christie JM (1967) Transmission electron microscope study of Brazil twins and dislocations experimentally produced in natural quartz. Phys Status Solidi 19:631–644

Morrison-Smith DJ, Paterson MS, Hobbs BE (1976) An electron microscope study of plastic deformation in single crystals of synthetic quartz. Tectonophysics 33:43–79

Nuttall RHD, Weil JA (1980) Two hydrogenic trapped-hole species in α-quartz. Solid State Commun 33:99–102

O'Keeffe M, Hyde BG (1978) On Si-O-Si configurations in silicates. Acta Crystallogr B 34:27–32

Paterson MS, Kekulawala KRSS (1979) The role of water in quartz deformation. Bull Mineral 102:92–98

Phakey PP (1967) Defects in quartz studied by transmission electron microscopy and x-ray diffraction topography. Ph D thesis Monash University, Australia

Retchford JA (1973) Plastic deformation of quartz. M Sc thesis Monash University, Australia

Shewmon PG (1963) Diffusion in solids. McGraw-Hill, New York

Tolansky S (1960) Surface microtopography. Longmans, London

Tolansky S (1968) Microstructures of surfaces using interferometry. Edward Arnold, London

Wood DL (1960) Infrared absorption of defects in quartz. J Phys Chem Solids 13:326–336

Received June 7, 1982